LETTER

https://doi.org/10.1038/s41586-018-0798-3

# Quantum Hall effect based on Weyl orbits in $Cd_3As_2$

Cheng Zhang[1,2,12], Yi Zhang[3,12], Xiang Yuan[1,2,12], Shiheng Lu[1,2], Jinglei Zhang[4], Awadhesh Narayan[5], Yanwen Liu[1,2], Huiqin Zhang[1,2], Zhuoliang Ni[1,2], Ran Liu[1,2], Eun Sang Choi[6], Alexey Suslov[6], Stefano Sanvito[7], Li Pi[4], Hai-Zhou Lu[8,9], Andrew C. Potter[10] & Faxian Xiu[1,2,11]*

**Discovered decades ago, the quantum Hall effect remains one of the most studied phenomena in condensed matter physics and is relevant for research areas such as topological phases, strong electron correlations and quantum computing[1–5]. The quantized electron transport that is characteristic of the quantum Hall effect typically originates from chiral edge states—ballistic conducting channels that emerge when two-dimensional electron systems are subjected to large magnetic fields[2]. However, whether the quantum Hall effect can be extended to higher dimensions without simply stacking two-dimensional systems is unknown. Here we report evidence of a new type of quantum Hall effect, based on Weyl orbits in nanostructures of the three-dimensional topological semimetal $Cd_3As_2$. The Weyl orbits consist of Fermi arcs (open arc-like surface states) on opposite surfaces of the sample connected by one-dimensional chiral Landau levels along the magnetic field through the bulk[6,7]. This transport through the bulk results in an additional contribution (compared to stacked two-dimensional systems and which depends on the sample thickness) to the quantum phase of the Weyl orbit. Consequently, chiral states can emerge even in the bulk. To measure these quantum phase shifts and search for the associated chiral modes in the bulk, we conduct transport experiments using wedge-shaped $Cd_3As_2$ nanostructures with variable thickness. We find that the quantum Hall transport is strongly modulated by the sample thickness. The dependence of the Landau levels on the magnitude and direction of the magnetic field and on the sample thickness agrees with theoretical predictions based on the modified Lifshitz–Onsager relation for the Weyl orbits. Nanostructures of topological semimetals thus provide a way of exploring quantum Hall physics in three-dimensional materials with enhanced tunability.**

The quantum Hall effect is important for probing electronic states via transport experiments and is a hallmark of two-dimensional (2D) electron systems[2,3]. It has been widely used in research and applications, including the metrological resistance standard and research on many-body problems[2,4,5,8]. By contrast, three-dimensional (3D) systems normally do not exhibit the quantum Hall effect owing to the band dispersion along the direction of the magnetic field, which smears the energy gap between the Landau levels. As an exception, the quantum Hall effect may occur in a 3D system when the Fermi level lies inside a gap[9–11], and scenarios involving either weak interlayer hopping or density-wave gaps have been proposed accordingly[11,12]. Over the years, several material systems, such as semiconductor superlattices[13], Bechgaard salts[14,15], $\eta$-$Mo_4O_{11}$ (ref. [16]), highly doped $Bi_2Se_3$ (ref. [17]), $EuMnBi_2$ (ref. [18]) and $ZrTe_5$ (ref. [19]), have been found to exhibit signatures of the quantum Hall effect in their 3D bulk forms. However, in these cases, the underlying physics resembles that of stacked 2D quantum Hall systems, and the corresponding systems can therefore be regarded as such.

Here we report the realization of a new type of quantum Hall effect based on Weyl orbits in nanostructures of the Dirac semimetal $Cd_3As_2$. Weyl orbits are inter-surface, 3D cyclotron orbits that consist of Fermi-arc surface states and bulk chiral Landau levels in Dirac and Weyl semimetal films under magnetic fields[6,20–22]. When driven into quantum Hall states, Weyl orbits exhibit chiral edge states that extend along the thickness ($z$) direction. Owing to the propagation process through the chiral Landau level, the Landau-level energy of a Weyl orbit is a function of both magnetic field and sample thickness. By using wedge-shaped samples, we show that the quantum Hall resistance is strongly modulated by a small variation in thickness (several nanometres). This spatially non-uniform quantum Hall resistance comes from the in-bulk chiral 'edge' states (which although they occur in the bulk rather than at an edge have the same physics as edge states) when the Landau levels shift with the variation in sample thickness and then intersect the Fermi level. The angular dependence of the quantum Hall resistance further reveals a connection between the Landau level and the $k$-space separation of pairs of Weyl nodes. These features highlight the Weyl-orbit nature of the quantum Hall effect in $Cd_3As_2$ nanostructures, opening up a new way of creating quantum Hall states in 3D systems.

Dirac and Weyl semimetals both have pairs of monopoles of the Berry curvature in 3D momentum space (also known as Weyl nodes). A typical example of a Dirac semimetal is $Cd_3As_2$ with two opposite pairs of Weyl nodes overlapping in the [001] axis[23–26]. When the 3D bulk is terminated by a 2D surface, exotic surface states appear in the form of Fermi arcs connecting the surface projections of pairs of Weyl nodes[27–30]. In the presence of a magnetic field, electrons following semi-classical equations of motion traverse a Fermi arc on the surface, tunnel along the bulk chiral Landau level to the opposing surface, where they continue their paths along the Fermi arc, and then tunnel through the bulk via the counter-propagating chiral Landau level back to the initial surface (Fig. 1a)[6]. This overall transport process forms a closed orbit, which behaves like a 2D state when projected on the surface, but with a unique bulk propagation process that gives rise to quantum oscillations, as observed in $Cd_3As_2$[21,22].

The quantum Hall effect is an extension of the semi-classical Shubnikov–de Haas oscillations in 2D systems. The chiral edge state that forms in the open edge of a quantum Hall system provides a ballistic transport channel and gives rise to the quantized Hall resistance (Fig. 1b)[2]. Similarly, for the Weyl orbit, the chiral edge state is predicted to emerge on the planar edge of a 3D Weyl or Dirac semimetal in a magnetic field[7] (Fig. 1c). The quantum Hall effect based on Weyl orbits is distinct from purely 2D quantum Hall effects, which have been widely studied previously, because the chiral edge state is extended along the out-of-plane ($z$) direction and intersects both the top and the bottom surfaces. The quantum Hall effect was recently observed in the surface states of $Cd_3As_2$ nanostructures[22,31], but it remains unclear whether it is due to the Weyl orbits or to the topological-insulator-type

[1]State Key Laboratory of Surface Physics and Department of Physics, Fudan University, Shanghai, China. [2]Collaborative Innovation Center of Advanced Microstructures, Nanjing, China. [3]Department of Physics, Cornell University, Ithaca, NY, USA. [4]Anhui Province Key Laboratory of Condensed Matter Physics at Extreme Conditions, High Magnetic Field Laboratory of the Chinese Academy of Sciences, Hefei, China. [5]Materials Theory, ETH Zurich, Zurich, Switzerland. [6]National High Magnetic Field Laboratory, Tallahassee, FL, USA. [7]School of Physics and CRANN Institute, Trinity College, Dublin, Ireland. [8]Shenzhen Institute for Quantum Science and Engineering and Department of Physics, Southern University of Science and Technology, Shenzhen, China. [9]Shenzhen Key Laboratory of Quantum Science and Engineering, Shenzhen, China. [10]Department of Physics, The University of Texas at Austin, Austin, TX, USA. [11]Institute for Nanoelectronic Devices and Quantum Computing, Fudan University, Shanghai, China. [12]These authors contributed equally: Cheng Zhang, Yi Zhang, Xiang Yuan. *e-mail: Faxian@fudan.edu.cn

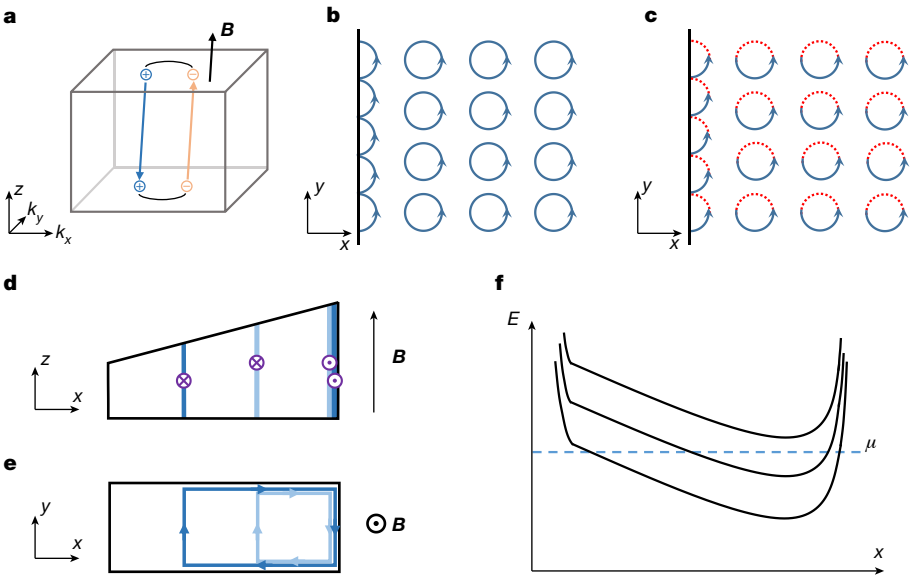


**Fig. 1 | The quantum Hall effect in Weyl orbits. a**, Illustration of the Weyl orbit under magnetic field ***B***. Two pairs of Weyl nodes of opposite chirality (+ and −) in the bulk are connected by Fermi arcs (black arcs) on two surfaces in the $k_x$–$k_y$ plane. Electrons propagate between the two surfaces (blue and orange arrows) in real space along the $z$ direction via the chiral Landau levels to complete the cyclotron motion. **b**, Cyclotron quantum Hall orbits of a 2D electron liquid in a magnetic field perpendicular to the $x$–$y$ plane. The chiral mode forms along the edge (left). **c**, Weyl orbits, which consist of surface Fermi arcs and bulk chiral Landau levels of a 3D Weyl semimetal in a magnetic field perpendicular to the $x$–$y$ plane. The solid blue and dashed red trajectories correspond to Fermi arcs on the top and bottom surfaces, respectively, which are connected through the chiral Landau levels in the bulk. **d**, A geometry with varying thickness $z$ along the $x$ direction. Two pairs of counter-propagating chiral modes (dark and light blue lines, with directions marked by the purple circles) occur on the side walls and at certain critical thicknesses, but with opposite Fermi velocities owing to the opposite signs of the thickness gradient. **e**, The same sample geometry as in **d** but showing the $x$–$y$ cross-section, where we have introduced a non-infinite width along the $y$ direction. Two chiral modes occur and close the loop of chiral modes. Possible chiral modes, corresponding to the lower Landau levels, around the exterior of the system are not shown. **f**, A schematic of the energy $E$ landscape of the Weyl orbits as a function of $x$ and therefore the thickness variation in **d**; different curves correspond to different Landau levels for the Weyl orbit. As the energy is pushed across the Fermi level $\mu$, gapless states occur at that particular $x$ position.

surface states that result from the chirality mixing effect of Dirac semimetals[6]. The latter corresponds to a conventional quantum Hall state without interaction between two surfaces.

Taking advantage of the recent progress in relation to the quantum Hall effect in $Cd_3As_2$ nanostructures[22], here we use samples with wedge geometries to detect directly the quantum phase from the bulk propagation in Weyl orbits. As illustrated in Fig. 1d, the sample has a thickness gradient along the $x$ direction. As a result, the accumulated quantum phase is position-dependent. Following the modified Lifshitz–Onsager relation in Weyl orbits[20], the quantization condition is also position-dependent, which results in a non-uniform filling factor $\upsilon$ along the $x$ direction. In the quantum Hall states, the quantization condition gives rise to chiral 'edge' states in the bulk that do not meet an edge, with $\upsilon$ changing by 1 at these edge states (Fig. 1d, e). The in-bulk chiral modes are dispersive along contours of equal thickness, localized along the $x$ direction and extend along the $z$ direction. However, despite extending over the entire thickness, each in-bulk chiral mode is a single mode, which is fundamentally different from what is observed in stacked 2D quantum Hall systems. These in-bulk chiral modes, and the edge modes that are induced by the sharp boundaries at the edges, all come from the intersection of a Landau level with a Fermi level (Fig. 1f). As the magnetic field changes, the real-space locations of the chiral modes also shift. For instance, an increase in the field strength reduces the contribution to the phase by the surface Fermi arcs, requiring the chiral mode to compensate by moving to positions with larger thickness until it annihilates with the counter-propagating mode at the edge. We carried out numerical simulations for the wedge geometry using a tight-binding model (see Supplementary Information for details). The local density of states that we obtain (Extended Data Fig. 1a) clearly demonstrates the existence of chiral modes at certain $x$ positions in the bulk—those at which the sample thickness satisfies the quantization relation. We also find that the in-bulk chiral modes are robust against moderate disorder, surface roughness, the Lifshitz energy and the hybridization effect due to breaking of the crystal symmetry (Extended Data Figs. 1–3). Using the wedge geometry, we can detect directly the thickness-variation-modulated chiral modes via the quantum Hall resistance in different regimes, confirming the Weyl-orbit nature of the quantum Hall states.

To probe in-bulk chiral modes experimentally, we carried out magneto-transport on $Cd_3As_2$ nanobelts (belt-shaped nanostructures) with slightly inclined top surfaces (see Methods). Using this geometry, we probe directly the thickness-dependent quantum phase within a single sample. By contrast, comparing the thickness effect from a series of samples of different thickness would require excluding sample-to-sample variations in Fermi energy. First, we selected a sample (sample 1) with a gradual change in thickness along the longitudinal direction (Fig. 2a–c) for transport measurements. Three sets of parallel Hall electrodes (1–2, 3–4 and 5–6) were fabricated on the sample, with thicknesses of about 59 nm, 66 nm and 71 nm, respectively, at the corresponding contact regions. On the basis of the analysis of Fig. 1d–f, we schematically show in Fig. 2d the anticipated distribution of quantum Hall chiral modes with such a thickness variation, which can be detected through the local quantum Hall resistance. In Fig. 2e we show the Hall resistance $R_{xy}$ measured at the three terminals. We find that although the classical Hall resistances for three pairs of electrodes are almost identical in the low-field regime, a systematic shift in the positions of the Hall plateaus for different thicknesses occurs as the systems enter the quantum Hall states. For a fixed filling factor, the Hall resistance in the thinner regimes enters the corresponding plateau at lower magnetic fields. That is to say, as the magnetic field increases, each Landau level is first depleted at the thinner positions of the sample. From the unequal filling factors detected at different terminals, we anticipate the existence of diverted chiral modes across the sample width at certain longitudinal positions. In Fig. 2f, in which we compare the two adjacent Hall resistances (1–2 and 3–4) with the corresponding longitudinal

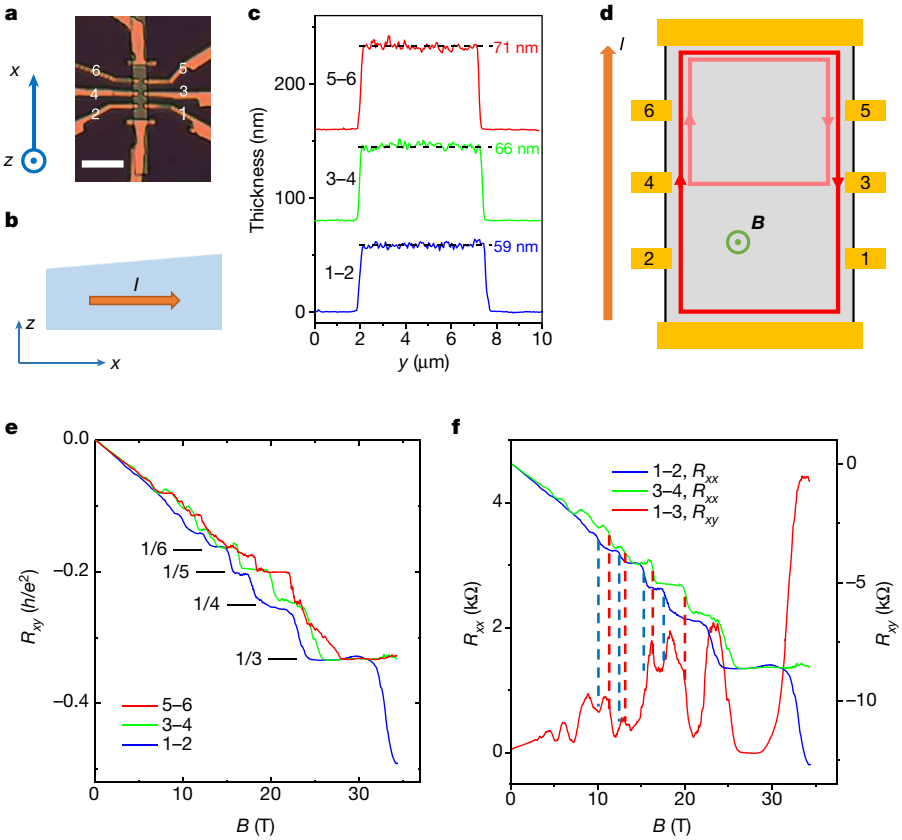


**Fig. 2 | Quantum Hall effect in sample 1, which is wedge-shaped along the *x* axis. a**, Optical image of the Hall bar device with terminals indexed. Scale bar, 15 μm. **b**, Schematic of the sample geometry. The sample thickness increases slightly along the *x* axis. The electric current *I* is applied along the *x* axis. **c**, Cross-sectional thickness profiles (offset for clarity) determined using atomic force microscopy near the three pairs of Hall electrodes (1–2, 3–4 and 5–6). The root-mean-square roughness in the thickness is roughly 2.0–2.6 nm. **d**, Schematic of the quantum Hall edge states for the wedge-shaped sample with a thickness gradient along the *x* axis. The electrodes are marked by the yellow boxes with the current *I* along the *x* direction. The light and dark red curves indicate the chiral modes. The magnetic field ***B*** is applied along the out-of-plane direction, as marked by the green circle. **e**, Hall resistance $R_{xy}$ ($h$, Planck constant; $e$, electronic charge) measured at the three pairs of Hall electrodes. The values of $R_{xy}$ at the plateaus are labelled. **f**, Comparison of the magnetoresistance $R_{xx}$ between terminals 1 and 3 (red, left axis) and $R_{xy}$ between terminals 1 and 2 (blue, right axis) and between terminals 3 and 4 (green, right axis). The Shubnikov–de Haas oscillation peaks in $R_{xx}$ are wide and cover the whole shifted regime between the two sets of Hall resistances. The vertical blue and red dashed lines mark the fields at which the Hall plateau changes, which agree with the peaks in $R_{xx}$.

magneto-resistance $R_{xx}$ (1–3), Shubnikov–de Haas oscillation peaks appear at the averaged positions of the Hall transitions, with relatively large peak widths.

We performed another set of experiments with a second sample (sample 2), in which the surface is tilted along the transverse direction ($y$ axis) with respect to the direction of current. As shown in Fig. 3a–c, the sample thickness on the right side (about 55 nm) is less than that on the left side (about 61 nm). Upon performing the same analysis as for sample 1, Fig. 3d schematically illustrates the mode distribution in sample 2, with emergent in-bulk chiral modes along the equal-thickness contours. Here, instead of changing with electrode position, the transition fields of quantum Hall plateaus shift when the direction of the magnetic field switches from being along the positive to the negative $z$ axis (Fig. 3e). The transitions of the filling factor from $\upsilon = 2$ to $\upsilon = 1$ occur at around 21 T and 28 T for the positive and negative $z$ directions, respectively, with a large difference of 7 T. This kind of non-uniform thickness along the $[44\bar{1}]$ direction ($y$ axis) is more commonly observed in as-grown $Cd_3As_2$ nanobelt samples. Note that here the asymmetric behaviour with respect to the magnetic field does not necessarily indicate the spontaneous breaking of time-reversal symmetry because the reciprocity of the conductance coefficients for four-terminal measurements would require both inverting the magnetic field direction and swapping the current and voltage terminals[32]. In a quantum Hall system, the chiral mode responsible for charge transport switches to its counter-propagating counterpart when the magnetic field switches direction. In our set-up, $R_{xy}$ measures the channel number at the right and left edges for the magnetic field in the positive and negative $z$ directions, respectively. Meanwhile, unlike the uniform-thickness case, in which $R_{xy}$ is not affected by a small misalignment of the electrodes in the localized state (because $R_{xx}$ is zero in the four-terminal measurement), the Hall plateau in Fig. 3e is interrupted by a peak in $R_{xx}$ between terminals 2 and 4 on the left edge at around −15.6 T. This finding suggests that one edge of the sample has entered the extended state while the other remains in the localized state at the corresponding field of the peak. In Fig. 3f–h we show $R_{xx}$ measured between terminals 1 and 3 and between terminals 2 and 4, and $R_{xy}$ measured between terminals 1 and 2. Two small peaks for terminals 2–4 are enlarged in Fig. 3i, and correspond to the filling factor transitions $\upsilon = 3$ to $\upsilon = 2$ and $\upsilon = 2$ to $\upsilon = 1$. Once again, in comparison to the right edge, the features on the thicker left edge are shifted to higher magnetic fields. Hence, the field-asymmetric behaviour of the Hall resistance in sample 2 is consistent with the Landau-level shift along the longitudinal directions in sample 1, suggesting a thickness-dependent Landau-level energy for the quantum Hall state in $Cd_3As_2$. By comparing the bulk quantum oscillations with in-plane magnetic fields (see Methods), we rule out the possible thickness-variation-induced change in the Fermi levels as the origin of the Landau-level shift.

We present in Fig. 4 another piece of evidence for the connection between the Landau level and the $k$-space separation of pairs of Weyl nodes. The separation of pairs of Weyl nodes (defined by the Weyl

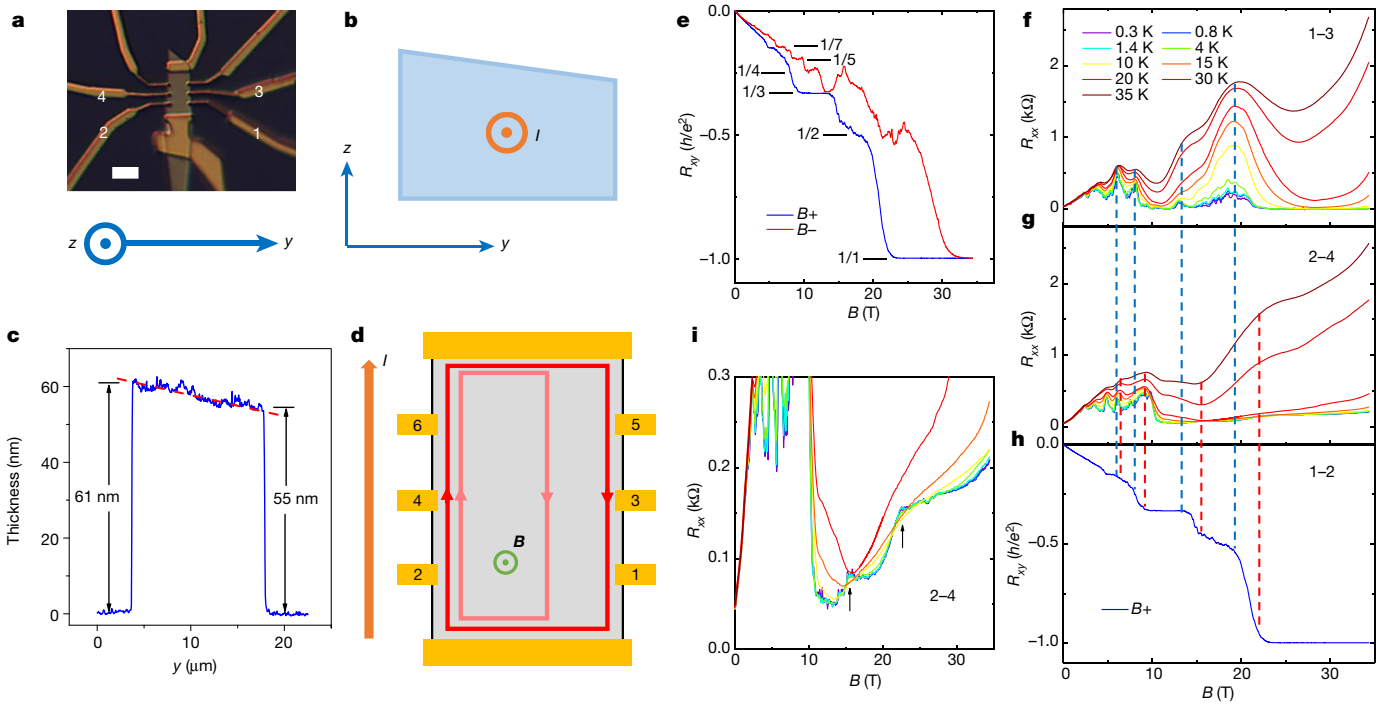


**Fig. 3 | Quantum Hall effect in sample 2, which is wedge-shaped along the *y* axis. a**, Optical image of the Hall bar device with terminals indexed. Scale bar, 15 μm. **b**, Schematic of the sample geometry. The sample thickness slightly increases along the *y* axis. **c**, Cross-sectional thickness profiles across the sample along the *y* axis. The red dashed line highlights the trend of the thickness variation. **d**, Schematic of the quantum Hall edge states for the wedge-shaped sample with a thickness gradient along the *y* axis. **e**, Hall resistance $R_{xy}$ measured with the magnetic field along the positive ($B+$) and negative ($B-$) *z* directions. The values of $R_{xy}$ at the plateaus are labelled. **f**–**h**, $R_{xx}$ measured between terminals 1 and 3 (**f**) and between terminals 2 and 4 (**g**), and $R_{xy}$ measured between terminals 1 and 2 (**h**), at different temperatures. Some shifts in the Landau levels are observed in the two sets of $R_{xx}$ curves (**f**, **g**), but the peak positions are generally located near the transition of $R_{xy}$. The vertical blue and red dashed lines mark the fields at which the Hall plateau changes, which agree with the peaks in $R_{xx}$. **i**, Enlarged view of **g**, with two small peaks marked by arrows.

vector $\boldsymbol{k}_w$) is along the [001] axis (Fig. 4a). When we tilted the magnetic field away from the normal direction in opposite directions (two tilting directions shown in Fig. 4b), we obtained different phase terms related to the Weyl vector. On the other hand, other potential mechanisms associated with the variable-thickness geometry, such as thickness-modulated changes in the Fermi level or band structure, would produce no distinction for the opposite tilting directions. In Fig. 4c we show a series of Hall resistances for sample 2 with the same tilting angle but opposite tilting directions (as illustrated in Fig. 4b). For low fields Hall resistance curves overlap, indicating no substantial deviation in the calibration of the zero-angle position in experiments. But several plateaus at high fields exhibit a notable difference between the two tilting directions. In Fig. 4d we summarize the shift in several Hall plateaus as a function of tilting angle. The shifts of even and odd Landau levels are generally opposite. We attribute this behaviour to the contributions from the phase shift due to $\boldsymbol{k}_w$ and from the Zeeman effect. Because the two contributions are coupled with the magnetic field direction in a similar manner, it is difficult to evaluate them separately. For the plateau corresponding to $\upsilon = 3$, the Landau-level shift saturates gradually as the angle increases and eventually starts to decrease. This decrease is possibly due to the Landau-level crossing behaviour when the splitting is changed by tilting the magnetic field.

A quantitative analysis of the thickness-dependent quantum phase shift can be carried out using the modified Lifshitz–Onsager relation for Weyl orbits. The phase shift in the inverse of the magnetic field can be expressed as (see Methods)

$$\Delta\left(\frac{1}{B_n}\right) = -\frac{e}{\hbar S_k}(k_{w\parallel} + 2k_{F\parallel})\Delta L$$

where $B_n$ is the magnetic field at which the *n*th Landau level is reached, $S_k$ is the momentum-space area enclosed by the surface Fermi arcs, and $k_{w\parallel}$ and $k_{F\parallel}$ are the separation between the pair of Weyl nodes and the Fermi wavevector, respectively, both along the magnetic field direction. In $Cd_3As_2$, there are two sets of overlapping Weyl cones in the bulk, with opposite Weyl vectors, as a result of the time-reversal and inversion symmetries. Owing to the lack of a chirality-sensitive approach, they could not be distinguished previously[22]. By contrast, the two Weyl orbits are split in quantum oscillations by the $\pm k_{F\parallel}$ contribution to the phase shift, and the second term from the $k_{F\parallel}$ contribution gives the overall thickness-dependent phase shift regardless of the chirality (Fig. 5a). From Figs. 2 and 3, we find that the thickness variation mainly induces a universal phase shift and the Landau-level shift is dominated by the contribution from $k_{F\parallel}$; the even–odd splitting between the Weyl orbits of opposite chirality is comparably smaller. For this reason, we define the Landau-level shift ratio as $\Delta(1/B_n)F_s$, which corresponds to phase changes of multiples of $2\pi$, where $F_s$ is the quantum oscillation frequency of the Weyl orbit (not including the splitting-induced frequency doubling). In Fig. 5b we plot the Landau-level shift ratio averaged over the even and odd Landau levels of different electrodes for several samples as a function of the respective differences between the sample thicknesses at the locations of the electrodes. By performing a linear fit to the data, we obtain a slope of 0.068, smaller than the theoretical value of $1/\pi$ expected from the expression for the phase shift. One reason for the deviation could be that the bulk Fermi surface is no longer isotropic at low energy because it is at high Fermi energy[24,33]. This would affect our estimate of $k_{F\parallel}$ using the in-plane bulk quantum oscillations, which gives the average Fermi wavevector of the $(1\bar{1}0)$ plane.

The type of quantum Hall effect described here, based on Weyl orbits, goes beyond the conventional scenario of stacking 2D quantum Hall planes. The quantum phase of the cyclotron Weyl orbits and the corresponding Landau levels depend on not only the magnetic field but also the sample thickness. In this context, it would be interesting to

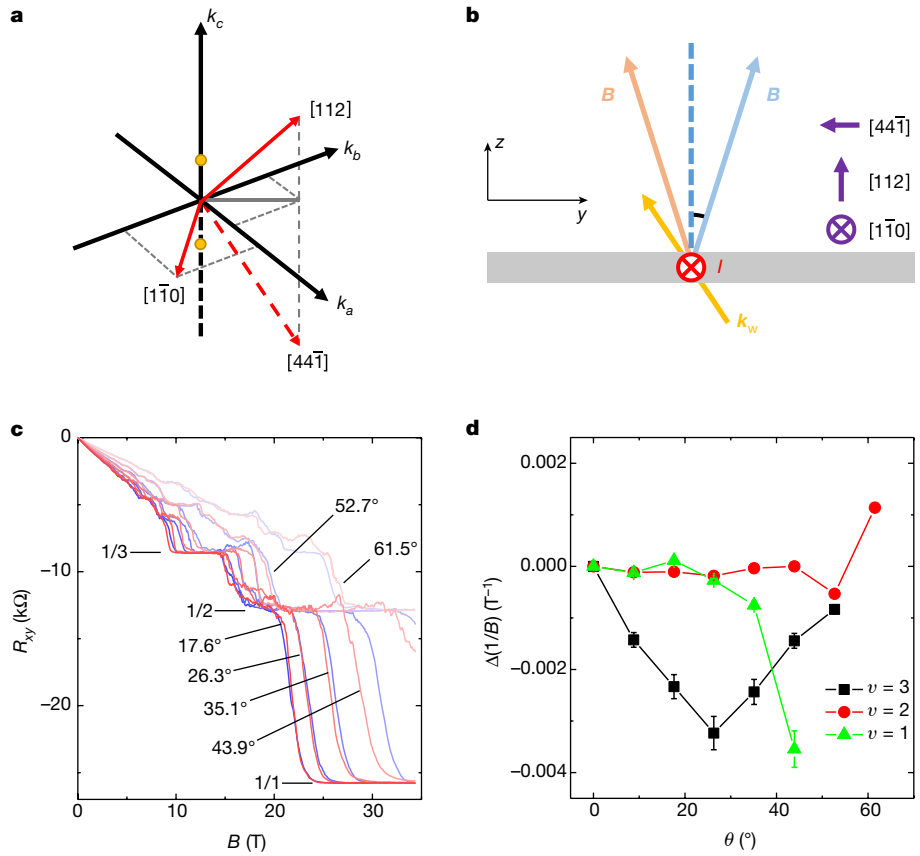


**Fig. 4 | Asymmetry in the Hall resistance when tilting along two opposite directions within the *y*–*z* plane. a**, Illustration of the positions of the Weyl nodes (yellow dots) of $Cd_3As_2$ in momentum (***k***) space. The Weyl nodes lie on the [001] direction; the direction normal to the surface of the $Cd_3As_2$ nanobelts is [112]. **b**, Measurement geometry used to distinguish the momentum- and real-space origins of the phase shift. The yellow arrow marked ($\boldsymbol{k}_w$) corresponds to the Weyl vector. The purple arrows denote the crystallographic directions. Tilting the magnetic field ***B*** by an angle $\theta$ along the two opposite directions shown will result in identical behaviour in real space, but yields different angles with respect to the Weyl vector $\boldsymbol{k}_w$. **c**, Hall resistance $R_{xy}$ of sample 2 for the same tilt angle but different tilting directions, as illustrated in **b**; blue and red lines correspond to positive and negative $\theta$, respectively, and different shades correspond to different $\theta$ (as labelled). The values of $R_{xy}$ at the plateaus are labelled. **d**, Angular dependence of the Landau-level shifts $\Delta(1/B)$ for different Hall plateaus (illustrated by the tilt angle $\theta$). Opposite Landau-level shifts take place for even and odd fillings $\upsilon$. The error bars represent the deviations in the shifts for different regimes in the transition.

investigate the real-space distribution of the chiral modes via scanning probe experiments and the effect of correlations with a higher magnetic field or lower carrier density. The interplay between topological Weyl and Dirac semimetals and quantum Hall physics will open up new research into topological phenomena and device applications in three dimensions beyond 2D electron systems.

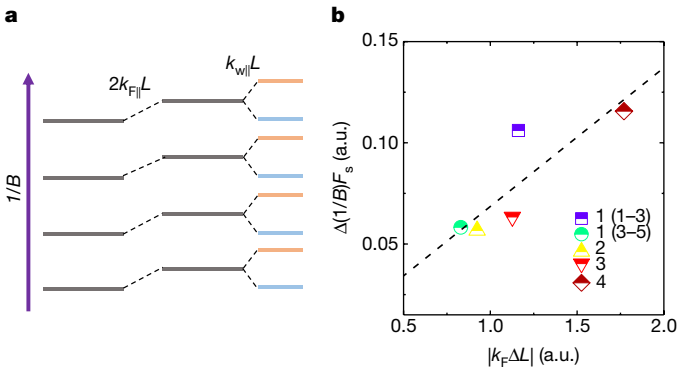


**Fig. 5 | Analysis of the Landau-level shift in Weyl orbits. a**, Schematic of the Landau-level shift process. The first transition corresponds to the global phase shift from $k_{F\|}$, which is independent of the chirality. The second transition (or splitting) corresponds to the phase shift from $k_{w\|}$, which splits the Shubnikov–de Haas oscillations from the two sets of degenerate Weyl orbits in $Cd_3As_2$. $L$ is the sample thickness. **b**, Quantitative analysis of the global phase shift $\Delta(1/B)$ in several samples. $\Delta L$ is the thickness variation. The overall trend follows a simple linear relationship (dashed line). a.u., arbitrary units.

## Online content

Any methods, additional references, Nature Research reporting summaries, source data, statements of data availability and associated accession codes are available at https://doi.org/10.1038/s41586-018-0798-3.

Received: 19 April 2018; Accepted: 24 October 2018;
Published online 17 December 2018.

1. Klitzing, K. v., Dorda, G. & Pepper, M. New method for high-accuracy determination of the fine-structure constant based on quantized Hall resistance. *Phys. Rev. Lett.* **45**, 494–497 (1980).
2. Cage, M. E. et al. *The Quantum Hall Effect* (Springer, Berlin, 2012).
3. Castro Neto, A. H., Guinea, F., Peres, N. M. R., Novoselov, K. S. & Geim, A. K. The electronic properties of graphene. *Rev. Mod. Phys.* **81**, 109–162 (2009).
4. Hasan, M. Z. & Kane, C. L. Colloquium: Topological insulators. *Rev. Mod. Phys.* **82**, 3045–3067 (2010).
5. Nayak, C., Simon, S. H., Stern, A., Freedman, M. & Das Sarma, S. Non-Abelian anyons and topological quantum computation. *Rev. Mod. Phys.* **80**, 1083–1159 (2008).
6. Potter, A. C., Kimchi, I. & Vishwanath, A. Quantum oscillations from surface Fermi arcs in Weyl and Dirac semimetals. *Nat. Commun.* **5**, 5161 (2014).
7. Wang, C. M., Sun, H.-P., Lu, H.-Z. & Xie, X. C. 3D quantum Hall effect of Fermi arc in topological semimetals. *Phys. Rev. Lett.* **119**, 136806 (2017).
8. Jeckelmann, B. & Jeanneret, B. The quantum Hall effect as an electrical resistance standard. *Rep. Prog. Phys.* **64**, 1603–1655 (2001).
9. Halperin, B. I. Possible states for a three-dimensional electron gas in a strong magnetic field. *Jpn. J. Appl. Phys.* **26**, 1913–1919 (1987).
10. Kohmoto, M., Halperin, B. I. & Wu, Y.-S. Diophantine equation for the three-dimensional quantum Hall effect. *Phys. Rev. B* **45**, 13488 (1992).

11. Koshino, M., Aoki, H., Kuroki, K., Kagoshima, S. & Osada, T. Hofstadter butterfly and integer quantum Hall effect in three dimensions. *Phys. Rev. Lett.* **86**, 1062–1065 (2001).
12. Bernevig, B. A., Hughes, T. L., Raghu, S. & Arovas, D. P. Theory of the three-dimensional quantum hall effect in graphite. *Phys. Rev. Lett.* **99**, 146804 (2007).
13. Störmer, H., Eisenstein, J., Gossard, A., Wiegmann, W. & Baldwin, K. Quantization of the Hall effect in an anisotropic three-dimensional electronic system. *Phys. Rev. Lett.* **56**, 85–88 (1986).
14. Cooper, J. et al. Quantized Hall effect and a new field-induced phase transition in the organic superconductor $(TMTSF)_2PF_6$. *Phys. Rev. Lett.* **63**, 1984–1987 (1989).
15. Hannahs, S., Brooks, J., Kang, W., Chiang, L. & Chaikin, P. Quantum Hall effect in a bulk crystal. *Phys. Rev. Lett.* **63**, 1988–1991 (1989).
16. Hill, S. et al. Bulk quantum Hall effect in $\eta$–$Mo_4O_{11}$. *Phys. Rev. B* **58**, 10778–10783 (1998).
17. Cao, H. et al. Quantized Hall effect and Shubnikov–de Haas oscillations in highly doped $Bi_2Se_3$: evidence for layered transport of bulk carriers. *Phys. Rev. Lett.* **108**, 216803 (2012).
18. Masuda, H. et al. Quantum Hall effect in a bulk antiferromagnet $EuMnBi_2$ with magnetically confined two-dimensional Dirac fermions. *Sci. Adv.* **2**, e1501117 (2016).
19. Liu, Y. et al. Zeeman splitting and dynamical mass generation in Dirac semimetal $ZrTe_5$. *Nat. Commun.* **7**, 12516 (2016).
20. Zhang, Y., Bulmash, D., Hosur, P., Potter, A. C. & Vishwanath, A. Quantum oscillations from generic surface Fermi arcs and bulk chiral modes in Weyl semimetals. *Sci. Rep.* **6**, 23741 (2016).
21. Moll, P. J. et al. Transport evidence for Fermi-arc-mediated chirality transfer in the Dirac semimetal $Cd_3As_2$. *Nature* **535**, 266–270 (2016).
22. Zhang, C. et al. Evolution of Weyl orbit and quantum Hall effect in Dirac semimetal $Cd_3As_2$. *Nat. Commun.* **8**, 1272 (2017).
23. Borisenko, S. et al. Experimental realization of a three-dimensional Dirac semimetal. *Phys. Rev. Lett.* **113**, 027603 (2014).
24. Wang, Z., Weng, H., Wu, Q., Dai, X. & Fang, Z. Three-dimensional Dirac semimetal and quantum transport in $Cd_3As_2$. *Phys. Rev. B* **88**, 125427 (2013).
25. Neupane, M. et al. Observation of a three-dimensional topological Dirac semimetal phase in high-mobility $Cd_3As_2$. *Nat. Commun.* **5**, 3786 (2014).
26. Liu, Z. K. et al. A stable three-dimensional topological Dirac semimetal $Cd_3As_2$. *Nat. Mater.* **13**, 677–681 (2014).
27. Wan, X., Turner, A. M., Vishwanath, A. & Savrasov, S. Y. Topological semimetal and Fermi-arc surface states in the electronic structure of pyrochlore iridates. *Phys. Rev. B* **83**, 205101 (2011).
28. Weng, H., Fang, C., Fang, Z., Bernevig, B. A. & Dai, X. Weyl semimetal phase in noncentrosymmetric transition-metal monophosphides. *Phys. Rev. X* **5**, 011029 (2015).
29. Xu, S.-Y. et al. Discovery of a Weyl fermion semimetal and topological Fermi arcs. *Science* **349**, 613–617 (2015).
30. Lv, B. et al. Experimental discovery of Weyl semimetal TaAs. *Phys. Rev. X* **5**, 031013 (2015).
31. Schumann, T. et al. Observation of the quantum Hall Effect in confined films of the three-dimensional Dirac semimetal $Cd_3As_2$. *Phys. Rev. Lett.* **120**, 016801 (2018).
32. Datta, S. *Electronic Transport in Mesoscopic Systems* Ch. 2 (Cambridge Univ. Press, Cambridge, 1997).
33. Feng, J. et al. Large linear magnetoresistance in Dirac semimetal $Cd_3As_2$ with Fermi surfaces close to the Dirac points. *Phys. Rev. B* **92**, 081306 (2015).


**Acknowledgements** F.X. was supported by the National Natural Science Foundation of China (grant numbers 61322407, 11474058, 61674040 and 11874116), the National Key Research and Development Program of China (grant numbers 2017YFA0303302 and 2018YFA0305601) and the National Young 1000 Talent Plan. Y.Z. was supported by NSF DMR-1308089 and a Bethe fellowship at Cornell University. J.Z. was supported by the Youth Innovation Promotion Association CAS (grant number 2018486) and the Users with Excellence Project of Hefei Science Center CAS (grant number 2018HSC-UE011). C.Z. and X.Y. were supported by the China Scholarships Council (CSC; grant numbers 201706100053 and 201706100054). We acknowledge discussions with Y.-M. Lu and Y. Yu. C.Z. thanks T. Song for helping with part of the atomic force microscope measurements. Part of the sample fabrication was performed at Fudan Nano-fabrication Laboratory. Part of the transport measurements was performed at the High Magnetic Field Laboratory (HMFL), CAS. A portion of this work was performed at the National High Magnetic Field Laboratory (USA), which is supported by NSF cooperative agreement numbers DMR-1644779 and DMR-1157490 and the state of Florida. H.L. was supported by the Guangdong Innovative and Entrepreneurial Research Team Program (grant number 2016ZT06D348), the National Key R&D Program (grant number 2016YFA0301700), the National Natural Science Foundation of China (grant number 11574127) and the Science, Technology, and Innovation Commission of Shenzhen Municipality (grant numbers ZDSYS20170303165926217 and JCYJ20170412152620376). A.N. acknowledges support from ETH Zurich. A.C.P. was supported by NSF DMR-1653007.

**Reviewer information** *Nature* thanks T. Das and the other anonymous reviewer(s) for their contribution to the peer review of this work.

**Author contributions** F.X. conceived the ideas and supervised the research. S.L., H.Z., Z.N. and R.L. synthetized the $Cd_3As_2$ nanobelts. C.Z. fabricated the devices. C.Z., X.Y., J.Z. and Y.L. carried out the high-magnetic-field transport measurements, with the help of L.P., E.S.C. and A.S. J.Z. designed the rotation probe and set up the measurement system for high-magnetic-field transport experiments in HMFL. C.Z. analysed the transport data. Y.Z., A.N., S.S., H.-Z.L. and A.C.P. provided theoretical support. C.Z., Y.Z. and F.X. wrote the paper, with input from all co-authors.

**Competing interests** The authors declare no competing interests.

**Additional information**

**Extended data** is available for this paper at https://doi.org/10.1038/s41586-018-0798-3.
**Supplementary information** is available for this paper at https://doi.org/10.1038/s41586-018-0798-3.
**Reprints and permissions information** is available at http://www.nature.com/reprints.
**Correspondence and requests for materials** should be addressed to F.X.

## METHODS

**Modified Lifshitz–Onsager relation in a Weyl orbit.** As derived in a phase-space quantization analysis[20], the Lifshitz–Onsager relation of a Weyl orbit is

$$\frac{1}{B}=\frac{2\pi e}{\hbar S_k}\left[n+\gamma-\frac{L}{2\pi}(k_{w\|}+2k_{F\|})\right]$$

where $n$ is an integer index for the Landau level, $L$ is the sample thickness, $\hbar = h/(2\pi)$ and $\gamma$ represents a constant phase offset generated from other quantum effects[20]. Compared to a conventional cyclotron orbit, the additional term $-L(k_{w\|}+2k_{F\|})/(2\pi)$ results from the phase accumulated during the propagation through the bulk, which gives the thickness dependence of the Landau-level energy and can be used as the signature of Weyl orbits[20]. However, isolating this phase from other parameters, such as the change in the Fermi surface in a quantum oscillation study, is difficult and a direct probe is still lacking in experiments. So far, the only evidence for this bulk propagating process is from a qualitative comparison of Shubnikov–de Haas oscillations between rectangular- and triangular-shaped $Cd_3As_2$ microstructures[21]. In the triangular case, the Weyl-orbit oscillations vanish owing to destructive interference from the large thickness variation.

**Finite thickness effect in $Cd_3As_2$ nanostructures.** The Fermi level interacts with both the surface Fermi arcs and the bulk state of the Weyl orbit. With a Fermi level away from the Weyl nodes, the electrons on the surface Fermi arcs may tunnel into the bulk before moving all the way to the projections of the Weyl node.

All bulk Landau levels, including the chiral mode, become continuous owing to the energy dispersion along the magnetic field (Extended Data Fig. 4a). This is very different from 2D systems such as graphene. Therefore, bulk Laudau levels cannot host quantized transport because there are too many modes. As discussed previously[22], to realize the quantum Hall effect, the bulk states need to have discrete energy levels as well. In our case, the finite quantum well structure in the $Cd_3As_2$ nanobelts forms a series of sub-bands, among which only a few bands are occupied, owing to the relatively low Fermi level (Extended Data Fig. 4b). Therefore, the band degeneracy for the Weyl orbit will be the sub-band number times the number of pairs of Weyl nodes. A sub-band number of 2 was observed previously, determined by the ratio between the quantum Hall mode number and the Landau-level index[22]. Here we choose thinner samples to reduce the degeneracy from the bulk sub-bands. The occupied sub-band number is determined to be 1 for sample 2 (possibly due to the smaller thickness and lower carrier density in sample 2) and 2 for sample 1. The different sub-band numbers explain why the quantum Hall resistance is very different whereas the surface and bulk oscillation frequencies (Fermi levels) are similar in these samples. Thinner samples can also help to suppress the conduction of the bulk channel.

Apart from the formation of bulk sub-bands, the effect of the finite (non-infinite) thickness in $Cd_3As_2$ nanostructures also induces a bandgap in the 2D limit[24]. Density function calculations were carried out using the Vienna ab initio simulation package (VASP)[34] with the Perdew–Burke–Ernzerhof exchange-correlation functional[35]. We used a plane-wave cut-off of 300 eV and a $4 \times 4 \times 2$ $\boldsymbol{k}$-point grid, with spin–orbit coupling included in all calculations. The experimentally determined $I4_1/acd$ crystal structure was used. The Hamiltonian was projected onto a basis of Cd 5*s* and As 4*p* states, using a Wannier projection[36]. We used this scheme to study the slab geometries in our experiments. As shown in Extended Data Fig. 4c–e, we find that for slabs with thicknesses of less than 10 nm, the bulk gap is substantial. The gap decreases rapidly as the thickness increases. For slabs with thicknesses of about 40 nm or 60 nm, the finite-thickness effect is negligible, with a gap value of less than 5 meV.

**Material growth.** The $Cd_3As_2$ nanobelts were grown by chemical vapour deposition using $Cd_3As_2$ powder as the precursor and argon as a carrier gas, similarly to previous reports[22,37,38]. The temperature was ramped rapidly to the growth temperature within 20 min, held constant for 30 min and then cooled naturally with the flow of argon. The precursor was placed in the hot centre of the furnace (around 760 °C) and the dull-polished quartz substrates were placed down-stream (around 200–250 °C). The as-grown $Cd_3As_2$ nanobelts adopt surfaces in the (112) crystal plane, with the longitudinal direction along the $[1\bar{1}0]$ axis—the same as the bulk crystals[39,40]. In our study, we specifically selected samples with inclined top surfaces to achieve non-uniform thicknesses. This type of $Cd_3As_2$ nanobelt forms naturally during chemical vapour deposition owing to differences in growth rates along different orientations, which originate from factors such as non-uniform flux flow[41]. The growth process results in a wedge-shaped cross-section, with the thickness varying slightly across the sample. We examine the sample-thickness profiles using atomic force microscopy. The carrier density and mobility for the as-grown nanobelts at low temperatures are usually of the order of $10^{17}$ $cm^{-3}$ and $10^5$ $cm^2\,V^{-1}\,s^{-1}$, respectively. These parameters enable easy access to the quantum Hall regime in transport.

Extended Data Fig. 5a shows a scanning electron microscopy (SEM) image of $Cd_3As_2$ nanostructures grown by chemical vapour deposition. Here, we selected one area with large nanobelts so that the wedge shape can be seen directly in side-wall SEM. As circled in Extended Data Fig. 5a, the wedge shape is very common in the as-grown nanobelts. The largest surface in the nanostructures is the (112) plane, consistent with previous reports[39,40]. Extended Data Fig. 5b shows the X-ray diffraction pattern of a large $Cd_3As_2$ belt with the (112) plane.

**Device fabrication and measurements.** $Cd_3As_2$ nanobelts were first transferred to pre-patterned silicon substrates with 285-nm thermal $SiO_2$. Samples with a thickness in the range 50–100 nm were chosen for transport measurements to suppress bulk conduction and to avoid inter-surface hybridization. The Hall bar devices were fabricated using electron beam lithography and wet-etched by standard buffered HF solution for about 3 s at the electrode area with deposition of Ti/Au (3 nm/150 nm) bilayers as the contact metal. The devices were pre-measured in a physical property measurement system (Quantum Design) to find low-carrier-density samples for high-magnetic-field experiments. High-magnetic-field transport experiments were carried out in water-cooled resistive magnets at the High Magnetic Field Laboratory in Hefei and the National High Magnetic Field Laboratory in Tallahassee. The high magnetic field (up to 34.4 T) in our experiment settings allows more quantum Hall plateaus to be resolved than in previous studies[22].

**Excluding other possible mechanisms for the thickness-dependent Landau-level shift.** Although the thickness dependence of Landau-level energy fits the scope of Weyl orbits, we now discuss whether there are other possible origins. Recent experiments have shown that with an out-of-plane magnetic field the quantum oscillations in $Cd_3As_2$ are dominated by the surface states for sample thicknesses of tens to a few hundreds of nanometres, especially for low-Fermi-level samples[21,22,42]. Apart from the Weyl-orbit scenario proposed here, the quantum Hall effect may also come from topological-insulator-type surface states. First, the connection between the steady change in sample thickness and the Landau-level shifts excludes randomly distributed defects for the spatially non-uniform quantum Hall resistance. Unlike Weyl orbits, topological-insulator-type surface states are generally not sensitive to the sample thickness unless there is inter-surface hybridization[43]. The thickness of our samples is still very large compared with the typical penetration depth of surface states. To confirm this, we rotated the magnetic field in-plane to eliminate the dominant surface quantum oscillations. Another set of quantum oscillations with a much smaller frequency (about 7.8 T) was detected in sample 2 and in other measured samples (Extended Data Figs. 6–8, Extended Data Table 1). This set corresponds to the bulk Fermi surface, indicating a well-defined bulk regime without strong hybridization between the top and bottom surface states. In addition, these quantum oscillations with the in-plane magnetic field show no thickness dependence in either sample (Extended Data Figs. 6e, 7a), suggesting that the Fermi energy does not vary with thickness and hence an interpretation in terms of a steady change in the Fermi energy with thickness is unlikely. Therefore, topological-insulator-type surface states cannot account for the strong thickness dependence of the Landau-level shift observed here.

**Discussion of proper sample thickness.** In Weyl-orbit assisted quantum Hall states, the overall sample thickness is very important. If the sample is too thick, the bulk conduction will overwhelm the surface transport and the electrons may suffer phase de-coherence over the long path across the thickness. If the sample is too thin, the strong quantum confinement effect and inter-surface hybridization will lead to a phase transition from a Dirac semimetal to a gapped insulator (or a topological insulator)[24], in which the Fermi arcs can be substantially deformed. Our density functional theory calculations (Extended Data Fig. 4) suggest that the bulk bandgap from the finite-thickness effect is prominent only below 10 nm and becomes negligible above 40 nm. Therefore, we estimate that the ideal thickness for the emergence of the non-trivial quantum Hall effect based on Weyl orbits in $Cd_3As_2$ should range from about 40 nm to roughly 100–200 nm. In addition, a relatively flat surface profile (the ratio between the surface roughness and the total thickness) is important to avoid strong phase de-coherence from thickness fluctuations. In contrast to the $Cd_3As_2$ nanostructures obtained by chemical vapour deposition[22] and focused ion beam fabrication[21], only bulk-state quantum oscillations are observed for 100-nm-thick thin films grown by pulsed laser deposition[44]. This is possibly related to the random terrace- or island-like features that typically form during thin-film deposition, especially for low-temperature deposition[45,46], which may induce extra scattering and phase de-coherence to the Weyl orbit. The surface roughness of our samples is only a few nanometres. Still, many small features of additional oscillations show up in $R_{xx}$ at very low temperatures, possibly corresponding to the contributions from areas of different thickness, and they smear out above 4 K (Extended Data Figs. 6d, 7c).

**Comparison of even and odd Landau levels.** By taking a closer look at the quantum Hall data, we find that not only the transition positions but also the plateau widths change simultaneously with thickness (Figs. 2d, 3d). Because the quantum

oscillations are periodic with respect to the inverse of the magnetic field $B$, we define the plateau width in terms of $1/B$ and plot the change in plateau width against the sample thickness. The even and odd Landau levels adopt opposite trends in terms of the decrease in thickness (Extended Data Fig. 9). This behaviour is usually associated with the change in the Zeeman splitting energy influenced by related parameters such as the magnetic field, which modifies the gap between the split Landau levels with opposite spins or pseudospins. In our case, the Zeeman effect and the phase-shift term from $k_{w\|}$ (discussed in the main text) will both lead to splitting behaviour of even and odd energy levels with the magnetic field. Although the $g$ factor of the surface state should not be affected by the sample thickness, the global Landau-level shift results in a change in the magnetic field, which modifies the Zeeman energy. However, this change in the field is typically small compared to the magnetic field itself (for example, $\Delta B \approx 4$ T for $B \approx 20$ T and $\upsilon = 5$ in sample 1). By ignoring the contribution of the Zeeman effect, we estimate $k_{w\|} = 0.154\ \mathrm{nm}^{-1}$ and $k_w = 0.188\ \mathrm{nm}^{-1}$ for $\Delta(1/B_n)F_s = |k_{w\|}\Delta L|/(2\pi^2)$. We find that this value of $k_w$ is four times smaller than the values estimated previously[21] from the size of the Fermi surface of the Weyl orbit (about $0.8\ \mathrm{nm}^{-1}$). This difference suggests that the $k$-space area enclosed by the Weyl orbit in $Cd_3As_2$ along the magnetic field direction is largely contributed by the curvature of the Fermi arc rather than the separation of the Weyl nodes.

## Data availability

The data shown in the plots and that support the findings of this study are available from the corresponding author on reasonable request.


34. Kresse, G. & Furthmüller, J. Efficiency of *ab-initio* total energy calculations for metals and semiconductors using a plane-wave basis set. *Comput. Mater. Sci.* **6**, 15–50 (1996).
35. Perdew, J. P., Burke, K. & Ernzerhof, M. Generalized gradient approximation made simple. *Phys. Rev. Lett.* **77**, 3865–3868 (1996).
36. Mostofi, A. A. et al. Wannier90: a tool for obtaining maximally-localised Wannier functions. *Comput. Phys. Commun.* **178**, 685–699 (2008).
37. Zhang, E. et al. Magnetotransport properties of $Cd_3As_2$ nanostructures. *ACS Nano* **9**, 8843–8850 (2015).
38. Zhang, C. et al. Room-temperature chiral charge pumping in Dirac semimetals. *Nat. Commun.* **8**, 13741 (2017).
39. Chen, Z.-G. et al. Scalable growth of high mobility Dirac semimetal $Cd_3As_2$ microbelts. *Nano Lett.* **15**, 5830–5834 (2015).
40. Ali, M. N. et al. The crystal and electronic structures of $Cd_3As_2$, the three-dimensional electronic analogue of graphene. *Inorg. Chem.* **53**, 4062–4067 (2014).
41. Koch, C. C. *Nanostructured Materials: Processing, Properties and Applications* Ch. 2 (William Andrew, Norwich, 2006).
42. Goyal, M. et al. Thickness dependence of the quantum Hall effect in films of the three-dimensional Dirac semimetal $Cd_3As_2$. *APL Mater.* **6**, 026105 (2018).
43. Zhang, Y. et al. Crossover of the three-dimensional topological insulator $Bi_2Se_3$ to the two-dimensional limit. *Nat. Phys.* **6**, 584–588 (2010).
44. Uchida, M. et al. Quantum Hall states observed in thin films of Dirac semimetal $Cd_3As_2$. *Nat. Commun.* **8**, 2274 (2017).
45. Heying, B. et al. Optimization of the surface morphologies and electron mobilities in GaN grown by plasma-assisted molecular beam epitaxy. *Appl. Phys. Lett.* **77**, 2885–2887 (2000).
46. Li, Y. Y. et al. Intrinsic topological insulator $Bi_2Te_3$ thin films on Si and their thickness limit. *Adv. Mater.* **22**, 4002–4007 (2010).

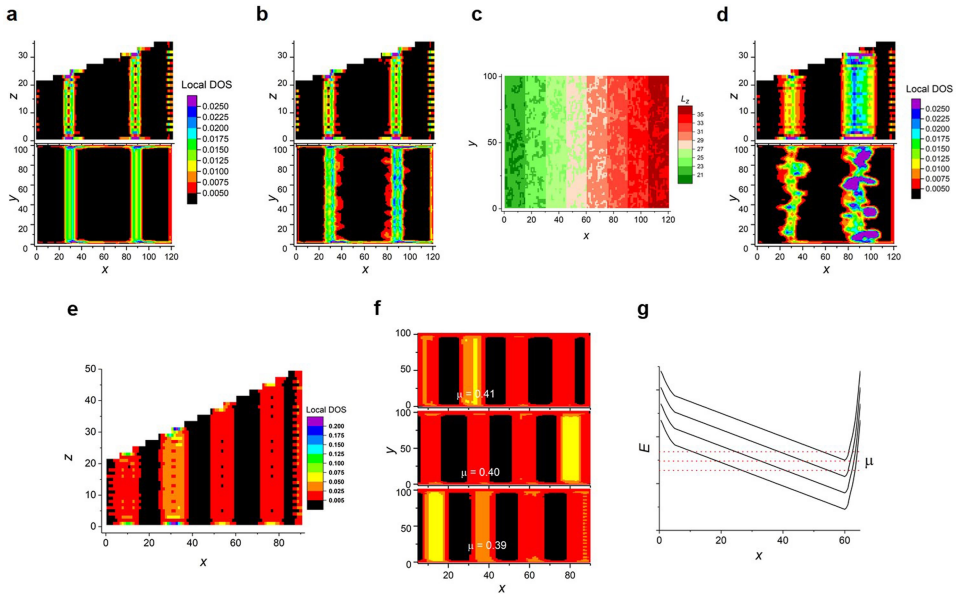


**Extended Data Fig. 1 | Numerical simulations of a wedge-shaped Weyl semimetal. a**, **b**, The local density of states (DOS; colour scale) in different cross-sections of a clean system with random impurities $W = 0$ (**a**) and a system with random impurities $W = 0.1$ (both in the bulk and on the surface; **b**), showing the location and extent of the modes. The system size is $L_x = 120$, $L_y = 100$ and $L_z \in [21, 35]$, with sharp side walls at both ends. The upper panels show trapezoidal $x$–$z$ cross-sections, with the local DOS averaged across $y \in [0.1L_y, 0.9L_y]$ to exclude contributions from the modes on the side walls at both ends in the $y$ direction. The lower panels show the $x$–$y$ cross-sections, with the local DOS averaged across the thickness $L_z$. We set the Fermi energy to $\mu = 0.4$. **c**, **d**, Real-space thickness profile in the $x$–$y$ plane ($L_z$, colour scale; **c**) and the local DOS (**d**). The settings are the same as in **a**, except that we consider a system with an uneven top surface (see **c**). **e**, Local DOS across the $x$–$z$ cross-section, averaged over $y \in [0.1L_y, 0.9L_y]$; $\mu = 0.41$. **f**, Local DOS in the $x$–$y$ cross-section, averaged over the thickness $L_z$, for Fermi energies of $\mu = 0.41$, $\mu = 0.40$ and $\mu = 0.39$. As the Fermi energy shifts, the $x$ position of the bulk modes moves accordingly. **g**, Schematic of the Landau levels. A chiral mode appears where the Landau level crosses the Fermi energy $\mu$ (red dotted lines). The energy profile also illustrates the origin of the counter-propagating chiral modes on the right side wall. The system size is $L_x = 90$, $L_y = 100$ and $L_z \in [21, 49]$; $W = 0$.

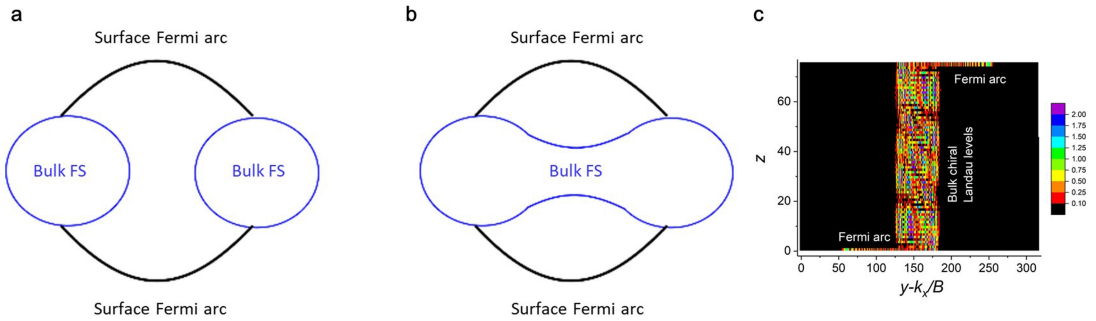


**Extended Data Fig. 2 | Illustration of Weyl orbits beyond the Lifshitz energy. a**, **b**, Surface Fermi arcs and projection of the bulk Fermi surfaces (FSs). Whereas the Fermi surfaces are separate and carry topologically quantized Berry curvatures in **a**, they merge into a single Fermi surface in **b**. Still, parts of the surface Fermi arcs remain well defined because the bulk is gapped at these surface wavevectors. **c**, Local DOS (colour scale) in the $y$–$z$ cross-section of the Weyl semimetal lattice model with a slab geometry and a magnetic field at cyclotron resonance. The Fermi energy $\mu = 1.05 > 1.0$ is beyond the Lifshitz transition in the bulk, yet we still observe clear signatures of the Weyl orbits consisting of both surface and bulk components.

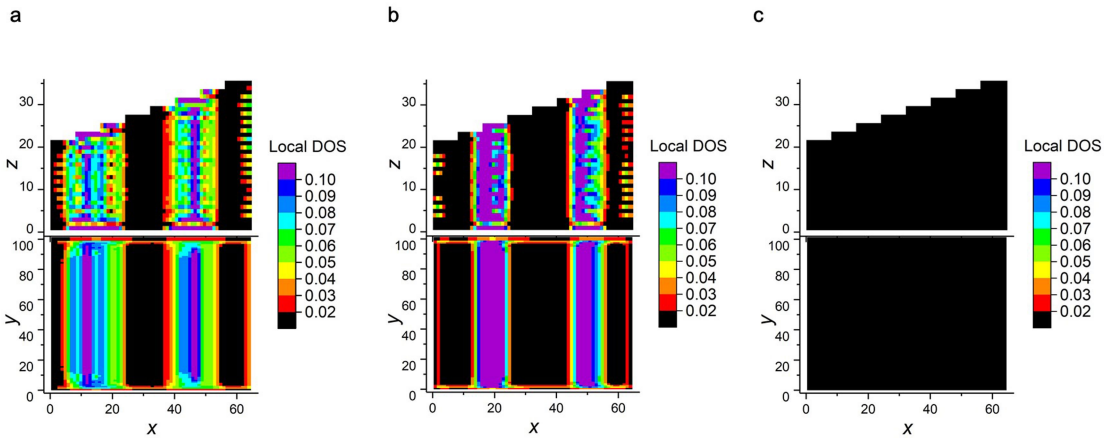


**Extended Data Fig. 3 | Numerical simulations of a wedge-shaped Dirac semimetal. a–c**, Local DOS (colour scale) of Dirac semimetal models showing the location and extent of the modes for different orbit hybridization amplitudes: $\Delta = 0.1$ in the two surface layers at the top and bottom surfaces (**a**); $\Delta = 0.05$ throughout the entire bulk (**b**); and $\Delta = 0.2$ (**c**). The system size is $L_x = 64$, $L_y = 100$ and $L_z \in [21, 35]$, with sharp side walls at both ends; $\mu = 0.4$, $W = 0$. The upper panels are the trapezoidal $x$–$z$ cross sections, with the local DOS averaged across $y \in [0.1L_y, 0.9L_y]$ to exclude contributions from the modes on the side walls at both ends in the $y$ direction. The lower panels show the $x$–$y$ cross sections, with the local DOS averaged across the thickness $L_z$. The chiral modes vanish completely in **c**.

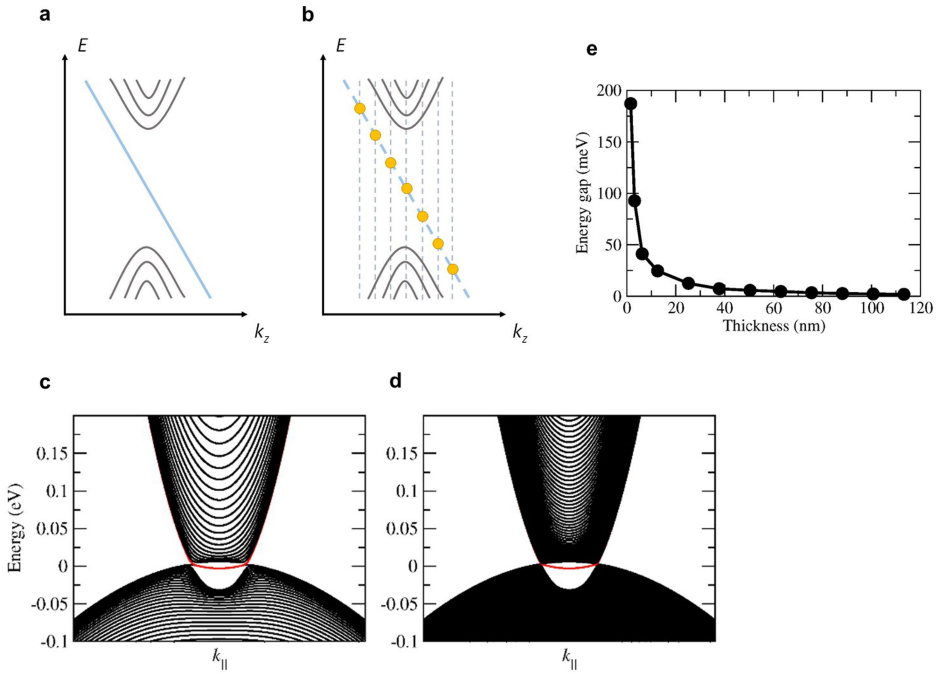


**Extended Data Fig. 4 | Finite-thickness effect in $Cd_3As_2$ slabs with (112) surface. a**, Bulk Landau-level spectrum for a Weyl cone without quantum confinement. The blue line denotes the gapless chiral Landau level. **b**, Bulk Landau-level spectrum for a Weyl cone with quantum confinement along the *z* axis. The yellow dots denote the discrete energy levels due to quantization in the finite-thickness quantum well. **c**–**d**, Representative band structures of $Cd_3As_2$ slabs with thicknesses of about 40 nm (**c**) and about 60 nm (**d**). The red lines denote the Fermi arc surface states, which persist for the 40-nm-thick films. **e**, Energy gap as a function of thickness. The finite-size effect is only important for slabs with thicknesses of less than 10 nm.

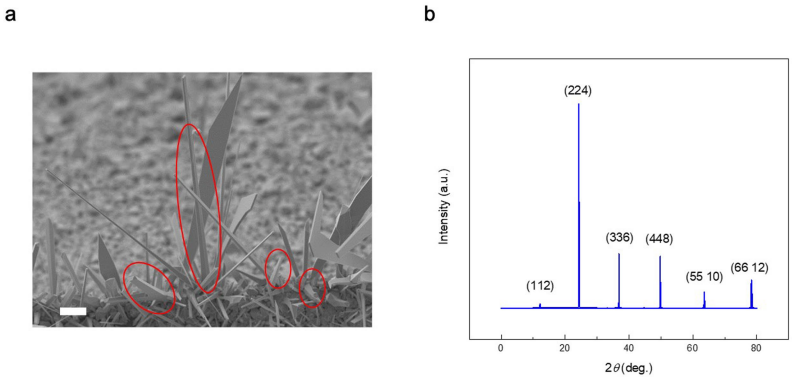


**Extended Data Fig. 5 | SEM image of $Cd_3As_2$ nanoplates. a**, A typical SEM image of as-grown $Cd_3As_2$ nanostructures. Scale bar, 100 μm. **b**, X-ray diffraction pattern of a large $Cd_3As_2$ belt with the (112) plane.

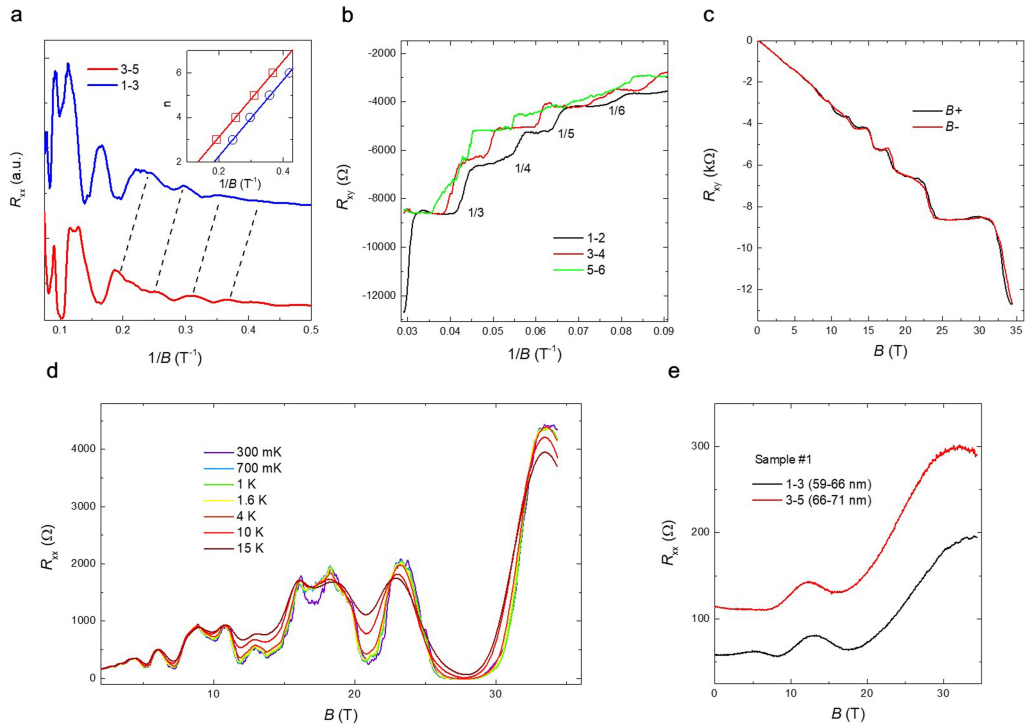


**Extended Data Fig. 6 | Additional transport data for sample 1.** **a**, Low-field oscillations of $R_{xx}$. The inset shows the corresponding Landau fan diagrams, the fitting curves of which have the same slope. The oscillation frequency is unchanged when measured at different terminals, as indicated by the parallel dashed black lines, suggesting that the Landau-level shift is not induced by the change in the size of the Fermi surface. The low-field oscillations are used to extract the Landau-level index. **b**, Hall resistance as a function of $1/B$. **c**, Comparison of the Hall resistance $R_{xy}$ at positive and negative magnetic fields for terminals 1–2, which is field-symmetric. **d**, Temperature dependence of $R_{xx}$. Small oscillation features are observed at very low temperature (below 1 K). Considering their periodicity and carrier mobility, and given that there is no corresponding feature in $R_{xy}$, these oscillations are not from the fractional quantum Hall effect. They probably come from regimes with different thickness, the Landau levels of which are shifted by the thickness-dependent phase term. **e**, Stack view of bulk quantum oscillations with in-plane magnetic field measured at different terminals of sample 1.

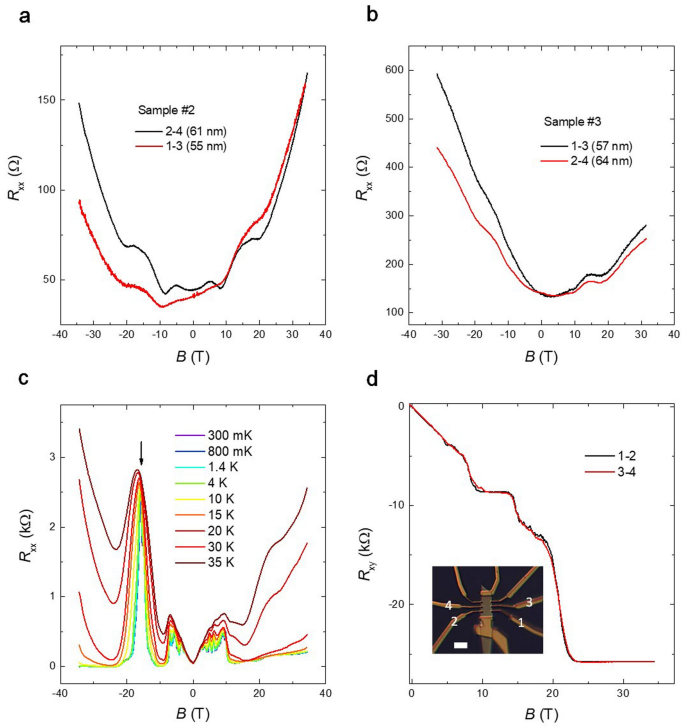


**Extended Data Fig. 7 | Additional transport data for samples 2 and 3.** **a**, **b**, Bulk quantum oscillations in samples 2 (**a**) and 3 (**b**) with the magnetic field applied in-plane. The oscillation positions are symmetric in $B$ and there is no shift between the two curves, which helps to exclude changes in the bulk band with thickness as the origin of the Landau-level shift. **c**, $R_{xx}$ measured at terminals 2–4 at different temperatures, which is also asymmetric under magnetic fields, similarly to Fig. 3e. The arrow marks the large oscillation peak, which is detected in $R_{xy}$ (Fig. 3e) at the same field. **d**, Hall resistance measured at two sets of Hall terminals along the $x$ axis with the same thickness profile. The inset shows an optical image of the Hall bar device with terminals indexed; scale bar, 15 μm.

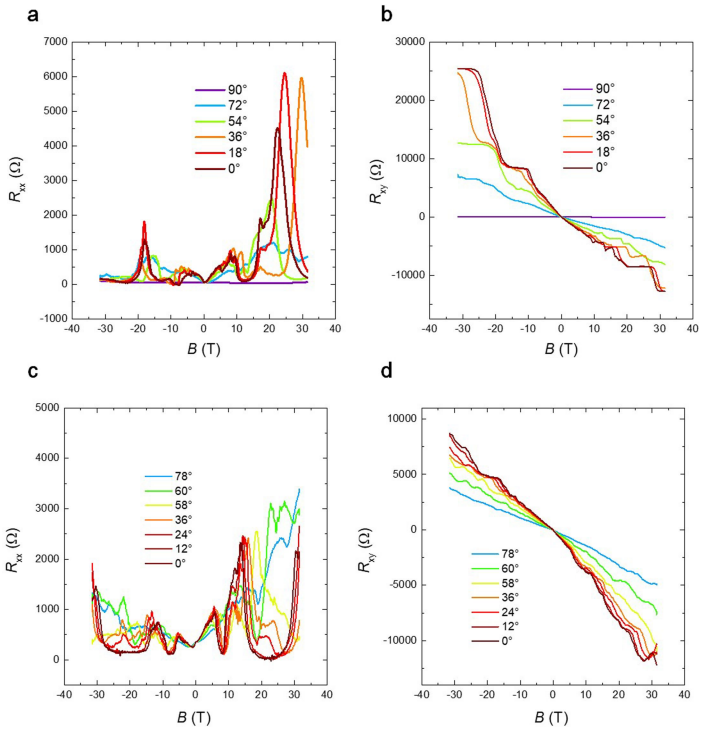


**Extended Data Fig. 8 | Transport data for samples 3 and 4. a**, **b**, Magnetotransport results for sample 3. **c**, **d**, Magnetotransport results for sample 4. Samples 3 and 4 both show strong asymmetric behaviour with magnetic field, similarly to sample 2.

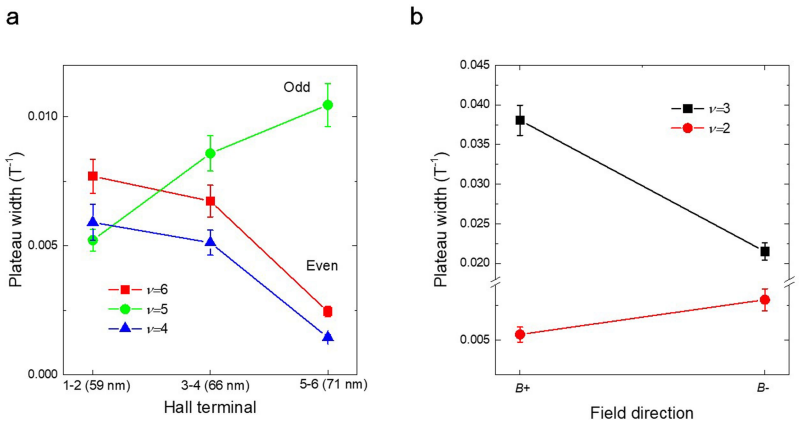


**Extended Data Fig. 9 | Change in the Landau-level plateau width with sample thickness and field direction. a**, Change in plateau width in sample 1 at different terminals. The trends for even and odd plateaus are opposite. **b**, Change in the plateau width for positive and negative magnetic fields. Here $\nu$ is the filling factor. The error bars represent the deviations of the transition field.

**Extended Data Table 1 | Summary of physical parameters for the four samples**

| Sample | $F_s$ (T) | $F_B$ (T) | $\Delta(1/B)$ ($T^{-1}$) | $L_{ave}$ (nm) | $\Delta L$ (nm) | $k_F$ ($nm^{-1}$) |
|---|---|---|---|---|---|---|
| #1 (Terminal 1-3) | 20.8 | 9.1 | 0.0051 | 63 | -7 | 0.166 |
| #1 (Terminal 3-5) | 20.8 | 9.1 | 0.0028 | 69 | -5 | 0.166 |
| #2 | 18.9 | 7.8 | 0.0030 | 58 | -6 | 0.154 |
| #3 | 19.2 | 8.5 | 0.0033 | 60 | -7 | 0.161 |
| #4 | 23.6 | 10.3 | 0.0053 | 75 | -10 | 0.177 |

$F_B$ and $F_S$ represent the bulk and surface oscillation frequency, respectively. $L_{ave}$ and $\Delta L$ are the average sample thickness and thickness variation, respectively.